Chinese Chemical Letters 35 (2024) 108341

Contents lists available at ScienceDirect

Chinese Chemical Letters

journal homepage: www.elsevier.com/locate/cclet

Enhancing the electrocatalytic performance of nitrate reduction to ammonia by *in-situ* nitrogen leaching

Mimi Fu, Yini Mao, Hua Wang, Wei Luo, Yimin Jiang, Wei Shen, Ming Li, Rongxing He*

College of Chemistry and Chemical Engineering, Southwest University, Chongqing 400715, China

ARTICLE INFO

Article history:
Received 2 February 2023
Revised 23 February 2023
Accepted 13 March 2023
Available online 15 March 2023

Keywords:
Co_4N
Nitrate reduction
In-situ nonmetal leaching
Nitrogen vacancy
Mechanism

ABSTRACT

Electrochemical nitrate reduction reaction (NITRR) is regarded as a "two birds-one stone" method for the treatment of nitrate contaminant in polluted water and the synthesis of valuable ammonia, which is retarded by the lack of highly reactive and selective electrocatalysts. Herein, for the first time, nickel foam supported Co_4N was designed as a high-performance NITRR catalyst by an *in-situ* nonmetal leaching-induced strategy. At the optimal potential, the Co_4N/NF catalyst achieves ultra-high Faraday efficiency and NH_3 selectivity of 95.4% and 99.4%, respectively. *Ex situ* X-ray absorption spectroscopy (XAS), together with other experiments powerfully reveal that the nitrogen vacancies produced by nitrogen leaching are stable and play a key role in boosting nitrate reduction to ammonia. Theoretical calculations confirm that Co_4N with abundant nitrogen vacancies can optimize the adsorption energies of NO_3^- and intermediates, lower the free energy (ΔG) of the potential-determining step ($^*NH_3$ to NH_3) and inhibit the formation of N-containing byproducts. In addition, we also conclude that the nitrogen vacancies can stabilize the adsorbed hydrogen, making H_2 quite difficult to produce, and lowering ΔG from $^*NO$ to $^*NOH$, which facilitates the selective reduction of nitrate. This study reveals significant insights about the *in-situ* nonmetal leaching to enhance the NITRR activity.

Nitrate (NO_3^-), as a common pollutant, is widely distributed in surface and ground water due to the improper use of N-containing fertilizers and the extensive discharge of industrial wastewater. The *in vivo* conversion of NO_3^- to NO_2^- can cause serious health problems such as blue baby syndrome, and even cancer [1,2]. Traditional biological, physical and chemical technologies such as biological denitrification, reverse osmosis, ion exchange and chemical reduction have been used for the treatment of nitrate for decades [3], but the harsh reaction conditions, complex operation process and high treatment cost have hindered their widespread application [4].

On the other hand, ammonia (NH_3) is a multifunctional compound, which can be used as an indispensable chemical feedstock for common chemical industry products [5–7]. Its high energy density (4.32 kWh/L) makes it a promising candidate for the next generation of carbon-free energy carriers [8]. The production of ammonia by traditional Haber-Bosch technology requires high temperature (400-600 °C) and high pressure (20-40 MPa), resulting in high energy consumption and costs [9]. Meanwhile, H_2, as one of the raw materials of the Haber-Bosch process, is mainly derived from fossil fuels. As the inevitable emission of a large amount of carbon dioxide in the process of hydrogen preparation from natural gas [10], new ammonia synthesis methods are being actively explored to replace the traditional Haber-Bosch process. In recent years, electrocatalytic reduction of N_2 to ammonia has received great attention. However, the NH_3 Faraday efficiency and selectivity are severely limited by the low solubility and strong triple bond (941 kJ/mol) of N_2 [11,12]. In contrast, the electrocatalytic reduction of NO_3^- to ammonia appears to be an extremely fascinating method for ammonia synthesis, benefiting from the high solubility and low N=O bond energy of nitrate (204 kJ/mol) [13]. Electrochemical nitrate reduction reaction (NITRR) plays the role of "two birds-one stone", which can realize the transformation of nitrate pollutants into value-added ammonia chemicals. It is well-known that the electrocatalytic reduction of NO_3^- to ammonia is a complex eight-electron and nine-proton transfer process, which inevitably generates NO_2^-, N_2 and other byproducts, resulting in low selectivity of ammonia. Furthermore, achieving the ideal yield rate and Faraday efficiency towards desired NH_3 has proved to be kinetically challenging, since hydrogen evolution reaction (HER) typically behaves as a predominant competitive reaction at more negative potentials. Therefore, electrocatalytic NITRR urgently requires high-performance electrocatalysts to improve the selectivity of am-

---

* Corresponding author.
E-mail address: herx@swu.edu.cn (R. He).

https://doi.org/10.1016/j.cclet.2023.108341
1001-8417/

monia and inhibit the evolution of hydrogen. In addition, compared with HER, OER and other electrocatalytic fields, there is still an urgent need to develop new and efficient electrocatalysts for nitrate reduction and further explore the mechanism of ammonia production.

In recent years, a series of strategies have been adopted to develop NITRR electrocatalysts with high activity and selectivity, among which vacancy engineering has proved to be an effective strategy. For example, oxygen vacancies (OVs) in TiO_2 nanotubes could capture nitrate and weaken the N-O bonding, thus improving NITRR activity [14]. Recently, it was reported that OVs and in-plane heterojunctions in Cu/CuO_x could synergistically regulate the electronic structure of active sites, thereby promoting the adsorption and further activation of nitrate [15]. OVs-rich oxides have been widely reported in the field of NITRR, but nitrides with abundant nitrogen vacancies (NVs) need to be further explored. Zhang *et al.* found that NVs could induce novel electronic states at the Fermi level, which is beneficial to nitrate adsorption and activation [16]. Therefore, it can be considered that the NVs in nitrides can effectively catalyze nitrate reduction. Up to now, the methods of creating vacancies generally include reduction, corrosion, heat treatment and plasma treatment [17]. It is critical to discover a strategy that can induce NVs more quickly and conveniently without additional processing.

In this work, Co_4N grown on Ni foam (NF), named as Co_4N/NF, was successfully synthesized and first used for nitrate reduction reaction. For comparison, two other catalytic materials, denoted as CoP/NF and Co_9S_8/NF, were fabricated using the same precursors. The Faradaic efficiency, NH_3 yield rate, and NH_3 selectivity of Co_4N/NF (95.4%, 0.2475 mmol h^{-1} cm^{-2}, and 99.4%) and CoP/NF (92.2%, 0.1823 mmol h^{-1} cm^{-2}, 95.2%) are obviously higher than those of Co_9S_8/NF (49.4%, 0.0157 mmol h^{-1} cm^{-2}, 62.5%) at −0.44 V *versus* the reversible hydrogen electrode (RHE). A series of experimental results unveil the reason why Co_4N/NF and CoP/NF perform better than Co_9S_8/NF, and confirm that the activity of NITRR is enhanced by the nonmetallic vacancies caused by the leaching of nonmetallic species under the condition of *in-situ* electrochemical reduction. Density functional theory (DFT) calculations suggest that the excellent performance of Co_4N/NF is closely correlated with NVs. It can be concluded that Co_4N with abundant NVs can reduce the NITRR reaction energy and H_2 generation by optimizing the adsorption energy of reactants/intermediates and enhancing the interaction between *H and the surface of Co_4N, thus achieving higher NITRR activity.

Co_4N/NF was synthesized by a two-step method. Typically, a Co(OH)F precursor grown on NF was synthesized by a hydrothermal method. Then, the as-synthesized precursor was annealed with urea at 400 °C for 3 h in Ar atmosphere (Fig. S1 in Supporting information). The crystal structures of the precursor and the target catalyst were investigated by X-ray diffraction (XRD). Fig. S2a (Supporting information) and Fig. 1a present the XRD patterns of Co(OH)F and Co_4N samples, respectively. The characteristic diffraction peaks previously indexed to Co(OH)F disappear and new peaks at 44.2°, 51.5° and 75.8° emerge after calcination. Such new diffraction peaks are perfectly matched with the (111), (200) and (220) crystal planes of Co_4N. The microstructure was characterized by scanning electron microscopy (SEM) and transmission electron microscopy (TEM). Fig. 1b shows the SEM image of the synthesized Co(OH)F/NF precursor. It can be seen that the whole surface of NF is densely and uniformly coated with flower-like Co(OH)F. For Co_4N/NF, the flower-like structure survives after nitridation but with rough surface (Fig. 1c). The TEM image of Co_4N (Fig. 1d) displays the morphology of the edge of a single micron-sized flower-like structure. The high-resolution TEM (HRTEM) image reveals the lattice fringes with the interplanar spacing of 0.204 nm, which can be indexed to the (111) plane of Co_4N (Fig. 1e). The corresponding selected area electron diffraction (SAED) pattern is also identified as the (111) plane of Co_4N (Fig. 1f). The high-angle annular dark-field scanning transmission electron microscopy (HAADF-STEM) and energy-dispersive X-ray spectroscopy (EDX) elemental mapping images are shown in Fig. 1g, indicating that Co and N elements present a uniform distribution in Co_4N. X-ray photoelectron spectroscopy (XPS) was investigated to further explore the chemical bonds and electronic states of Co_4N/NF and the results are displayed in Fig. S2b (Supporting information) and Figs. 1h and i. Fig. 1h shows the XPS Co 2p spectrum of Co_4N/NF, it can be deconvoluted into multiple types of peaks. The peaks of about 780.3 and 796.1 eV are ascribed to the Co-Co bonds, while two peaks centered at 781.6 and 797.3 eV should be attributed to the Co-N bonds [18]. The results demonstrate that there are two kinds of coordination environments of Co species in Co_4N. As shown in Fig. 1i, the high-resolution N 1s spectrum at 398.8 eV can be compatible with the Co-N bonds [19]. Therefore, the above results clearly confirm the successful synthesis of Co_4N material.

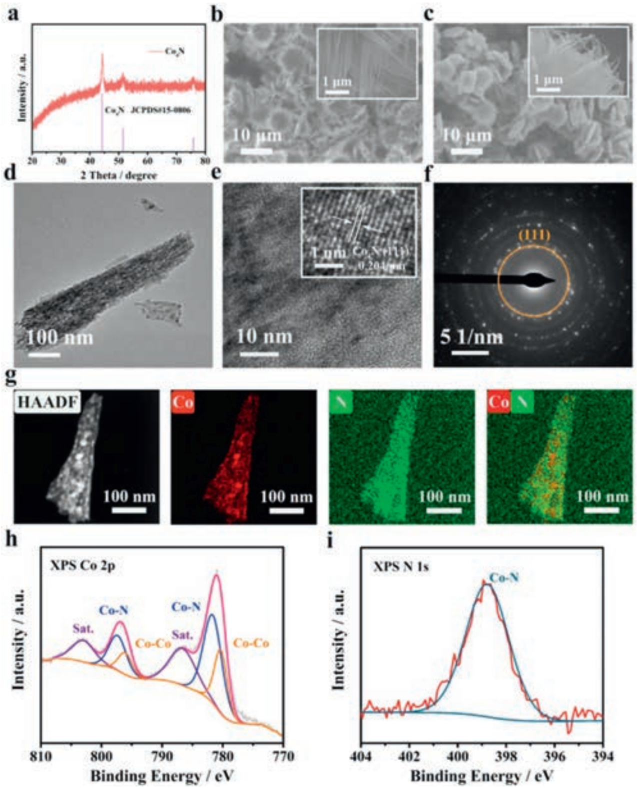

Fig. 1. (a) XRD pattern of Co_4N. (b) SEM image of Co(OH)F/NF. (c) SEM image of Co_4N/NF. (d) Low-resolution TEM image and (e) high-resolution TEM image of Co_4N. (f) SAED pattern of Co_4N. (g) HAADF-STEM image and the element mapping images of the Co_4N catalyst. (h) XPS Co 2p and (i) N 1s spectra of Co_4N/NF.

To investigate the NITRR performance of the Co_4N/NF electrocatalyst, an H-type electrolytic cell containing 0.5 mol/L K_2SO_4 and 200 ppm NO_3^--N was used. Co_4N/NF, platinum gauze, and saturated Ag/AgCl electrode were used as the working, counter, and reference electrodes, respectively. For convenience of comparison, all potentials reported in this work were converted to the RHE according to the following formula, $E(vs.\ \text{RHE}) = E(vs.\ \text{Ag/AgCl}) + 0.059 \times \text{pH} + 0.197$. The electrochemical nitrate reduction was tested at various potentials ranging from −0.29 V to −0.59 V *vs.* RHE. The reactant and products including NO_3^-, NH_3 and NO_2^- were detected by colorimetric methods, and the corresponding ultraviolet-visible (UV-vis) adsorption spectra with concentration-absorbance calibration curves are plotted in Figs. S3-S5 (Supporting information). Fig. 2a shows the linear sweep

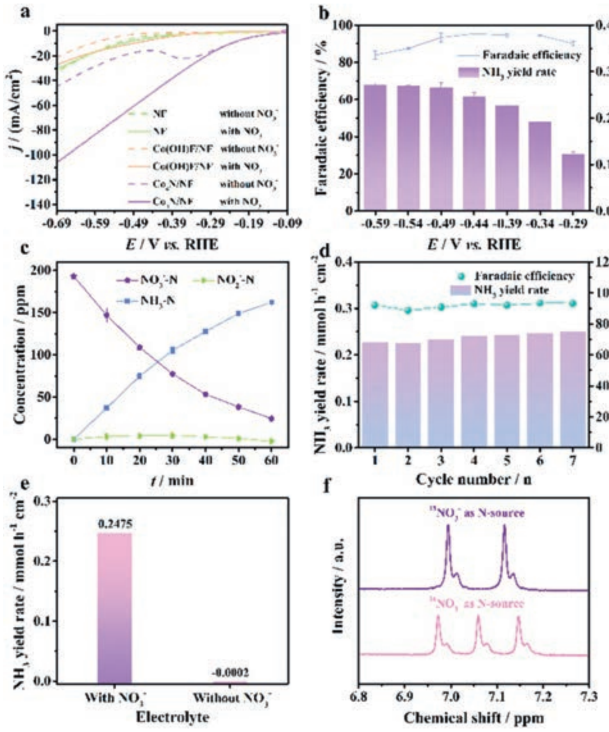

Fig. 2. (a) LSV curves of NF, Co(OH)F/NF and Co_4N/NF at 500 rpm in 0.5 mol/L K_2SO_4 electrolyte with and without 200 ppm NO_3^-. (b) Potential-dependent Faradaic efficiency and yield rate of ammonia over Co_4N/NF. (c) Time-dependent concentration change of NO_3^-, NH_3 and NO_2^- over Co_4N/NF at −0.44 V *vs.* RHE. (d) The stability test of Co_4N/NF at −0.44 V *vs.* RHE. (e) Calculated ammonia yield rate of Co_4N/NF in 0.5 mol/L K_2SO_4 electrolyte with and without 200 ppm NO_3^-. (f) ^1H NMR spectra of the electrolyte after NITRR tests at −0.44 V *vs.* RHE using $^{15}NO_3^-$ and $^{14}NO_3^-$ as the feeding nitrogen source.

voltammetry (LSV) curves of different electrodes (NF, Co(OH)F/NF, Co_4N/NF) with (solid line) and without (dash line) NO_3^- at a scan rate of 5 mV/s. The blank NF performs relatively low current density both in the presence and absence of NO_3^-, proving that it has almost no NITRR activity and HER activity at low overpotential. The current density of Co(OH)F/NF shows no significant increase in 0.5 mol/L K_2SO_4 electrolyte with 200 ppm NO_3^--N, indicating its poor NITRR activity. Compared with the substrate and the precursor, the significantly increased current density of Co_4N/NF in the electrolyte with nitrate compared to without nitrate at the same overpotential, implying the superior catalytic activity of Co_4N/NF toward NITRR. The reduction peak in the figure may be the reduction peak of Co unrelated to nitrate reduction, as it appears on the LSV curve in blank K_2SO_4 electrolyte. This peak disappears in the presence of NO_3^-, possibly due to the large current density response of Co_4N to nitrate reduction, covering the peak. To further investigate the catalytic performance of Co_4N/NF, chronoamperometry (CA) tests were performed at various potentials (−0.29 ∼ −0.59 V *vs.* RHE). As shown in Fig. 2b and Fig. S6 (Supporting information), with the decrease of cathodic potential, the Faradaic efficiency and selectivity of ammonia display a volcanic shape curve while the NH_3 yield rate gradually increases and tends to be stable. The change trend of NO_3^- conversion rate is similar to that of NH_3 yield rate. The Faradaic efficiency and selectivity of ammonia reached their respective maximum at −0.44 V *vs.* RHE, so it was determined as the optimal potential. At −0.44 V *vs.* RHE, the Faradaic efficiency, NH_3 yield rate, conversion rate of NO_3^-, and NH_3 selectivity of Co_4N/NF are 95.4%, 0.2475 mmol h^{-1} cm^{-2}, 89.5%, and 99.4%, respectively. The yield rate of NH_3 is much higher than that of Co(OH)F/NF (0.0169 mmol h^{-1} cm^{-2}) and NF (0.0041 mmol h^{-1} cm^{-2}) (Fig. S7 in Supporting information), demonstrating that Co_4N/NF catalyzes the conversion of NO_3^- to NH_3 effectively. The Faraday efficiency and selectivity of Co_4N/NF are superior to or comparable to most other reported NITRR catalysts or vacancy engineering related catalysts (Tables S1 and S2 in Supporting information). The time-dependent concentration curves of NO_3^-, NH_3 and NO_2^- were recorded at −0.44 V *vs.* RHE. With the extension of reduction time, the concentration of NO_3^- gradually decreases, and the concentration of NH_3 displays a completely opposite trend, indicating that ammonia is produced by the reduction of nitrate (Fig. 2c). Meanwhile, the concentration of NO_2^- is extremely low throughout the reaction process, suggesting that the production of NO_2^- as a byproduct is suppressed, which improves the selectivity of NH_3. As illustrated in Figs. S8 and S9 (Supporting information) and Fig. 2d, we also performed the consecutive recycling tests at −0.44 V *vs.* RHE to evaluate the durability of the prepared catalyst. Fig. S8 shows the chronoamperometric curves, the current density recovers immediately when the electrolyte is refreshed. After seven consecutive cycles, the Faradaic efficiency, NH_3 yield rate, conversion rate of NO_3^-, and NH_3 selectivity can remain stable, proving the outstanding stability of Co_4N/NF under neutral condition (Fig. 2d and Fig. S9). We also investigated the effect of some ions (CO_3^{2-}, Na^+, Cl^-, ClO_4^-, HCO_3^-, Li^+) commonly found in actual nitrate wastewater on the NITRR activity of Co_4N/NF. As shown in Figs. S10 and S11 (Supporting information), our catalyst can still maintain high NITRR activity when these ions coexist. In order to eliminate external interference, the ammonia yield of Co_4N/NF was determined after electroreduction in a nitrate-free blank electrolyte. As shown in Fig. 2e, no ammonia can be detected in the absence of NO_3^-, indicating that the detected ammonia originates from the added nitrate. We also conducted isotope labeling experiments to strengthen the result described above [20–22]. As shown in Fig. 2f, when the reactant is $K^{14}NO_3$, the ^1H NMR spectra show representative triple peaks of $^{14}NH_4^+$, while typical double peaks of $^{15}NH_4^+$ can be detected if the reactant is replaced by $K^{15}NO_3$ [23,24]. No significant $^{14}NH_4^+$ can be observed when $K^{15}NO_3$ is used, confirming that the produced ammonia is completely evolved from the electrochemical reduction of NO_3^- rather than external interference.

A series of comparative experiments before and after NITRR tests were conducted to reveal the origin of the superior catalytic performance of Co_4N/NF. The electrochemical active surface areas (ECSA) of Co_4N and Co(OH)F can be obtained by the double-layer capacitances (Figs. S12a-c in Supporting information). It is found that the ECSA value of Co_4N is 395 cm^{-2}, about 20 times that of Co(OH)F (20 cm^{-2}), which facilitates the reduction of nitrate. After NITRR tests, the morphology remains roughly unchanged. Interestingly, the surfaces of Co_4N/NF become rougher and completely covered by nanosheets after NO_3^- reduction reaction, thus exposing more active sites (Fig. 3a and Fig. S13 in Supporting information). The electronic structure of electrocatalysts affects their intrinsic activity. XPS analysis was performed to probe the changes of Co_4N before and after NITRR tests. As presented in Fig. 3b, the peaks in the low and high binding energy zones can be attributed to Co $2p_{3/2}$ and Co $2p_{1/2}$, respectively. After NITRR tests, the binding energy of Co 2p appears significantly negative shifts. Simultaneously, the high-resolution Co 2p and N 1s spectra suggest a significant decrease of the N/Co atomic ratio from 0.381 to 0.129 after NITRR, indicating the decreased coordination number of Co centers due to the leaching of nitrogen species (Fig. 3c). As shown in Fig. S14 (Supporting information), no other diffraction peaks are detected except the characteristic peaks of Co_4N, demonstrating that the major phase is still Co_4N during NITRR process. Thus, although about two-thirds of the nitrogen is leached from the Co_4N, the crystalline framework is not damaged and no phase change occurs. Nitrogen leaching results in a large number of NVs,

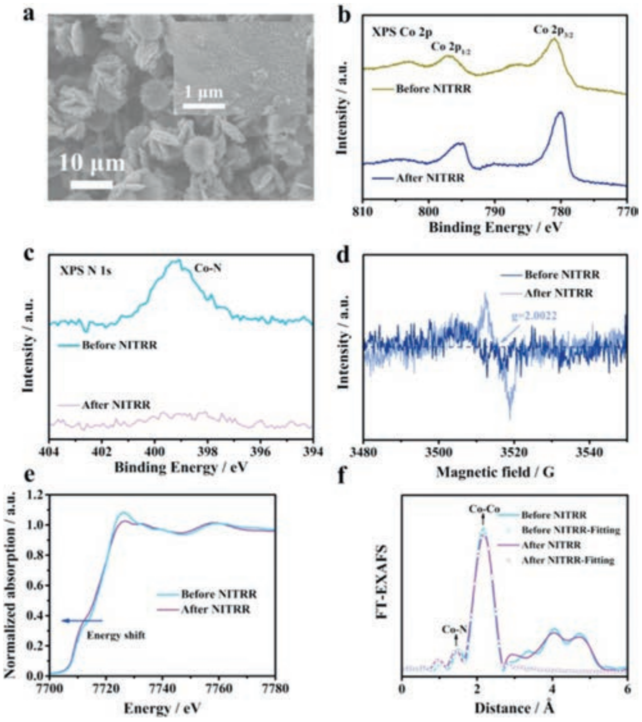

Fig. 3. (a) SEM image of Co_4N/NF after NITRR tests. (b) XPS Co 2p and (c) N 1s spectra of Co_4N/NF before and after NITRR tests. (d) EPR spectra of Co_4N before and after NITRR tests. (e) XANES and (f) EXAFS spectra of Co_4N/NF before and after NITRR tests.

as confirmed by Electron paramagnetic resonance (EPR) tests. According to Fig. 3d, the EPR signal at ~2.0022 is detected in Co_4N after NITRR, proving that NVs are introduced by *in-situ* electrochemical reduction, that is, nitrogen dissolution induced abundant nitrogen vacancies [25]. *Ex situ* X-ray absorption near-edge structure (XANES) and extended X-ray absorption fine-structure (EXAFS) spectra were carried out to further determine the fine structure of Co_4N and elucidate the catalytic mechanism. As exhibited in Fig. 3e, the XANES spectra show that the absorption threshold position of Co_4N after NITRR tests moves towards lower energy compared to that of Co_4N before NITRR tests, implying a slight decrease in the oxidation state of Co. The EXAFS spectra of the Co_4N catalyst before and after NITRR tests are shown in Fig. 3f. For the EXAFS spectrum of pre-test Co_4N, the two peaks at approximately 1.5 and 2.2 Å can be attributed to Co-N and Co-Co bonds, respectively [26]. It can be seen that the intensity of the Co-N shell decreases after NITRR tests, indicating that the coordination of Co centers is not saturated and the formation of NVs due to the dissolution of nitrogen species [11]. The results of XANES and EXAFS jointly clarify that the oxidation state and coordination number of Co centers decrease because of the leaching of nitrogen, which is in good agreement with the XPS conclusion. Fig. S15 (Supporting information) shows the Faraday efficiency-cycle number curve of Co_4N/NF at −0.44 V *vs.* RHE by 9 cycles. It is found that with the increase of reaction time, Faraday efficiency gradually increases and eventually tends to be stable, indicating a positive correlation between Faraday efficiency and nitrogen leaching within a certain time range at the beginning. It also indicates from the side that the ultra-high selectivity of Co_4N/NF electrocatalyst is attributable to the nitrogen vacancy generated by *in-situ* nitrogen leaching. The above results enable us to infer that the superior NITRR activity can be attributed to the following two aspects. First, the original large-size morphology is transformed into small-size nanosheets during the NITRR process, and more active sites are exposed. Second, the introduction of NVs owing to nitrogen leaching, which may be the main reason for the superior catalytic performance.

CoP/NF and Co_9S_8/NF were synthesized to further verify the hypothesis that potential-driven leaching of nonmetals into the electrolyte enhances nitrate reduction activity under *in-situ* electrochemical reduction conditions. The SEM images of CoP/NF and Co_9S_8/NF are presented in Fig. S16 (Supporting information). Fig. S17 (Supporting information) shows the XRD patterns of CoP and Co_9S_8, displaying no impurity peaks except the peaks of CoP and Co_9S_8 respectively, indicating the successful synthesis of the target catalysts. Fig. S18 (Supporting information) presents the XPS spectra of CoP/NF. Specifically, the Co 2p peaks at the binding energies of 778.9 and 793.9 eV should be assigned to the Co-P bonds, the peaks at 782.3 and 798.4 eV are ascribed to the Co-O bonds, which are derived from surface oxidation [27]. Meanwhile, the high-resolution P 2p spectrum displays three obvious P $2p_{3/2}$, P $2p_{1/2}$ and P-O signals, which is consistent with the results of Co 2p spectrum. As depicted in Fig. S19 (Supporting information), the high-resolution Co 2p and S 2p spectra of Co_9S_8/NF are fitted. The Co 2p spectrum can be fitted as Co^{3+} and Co^{2+}, the peaks at 778.4 and 793.3 eV are assigned to Co^{3+}, while the peaks at 781.1 and 797.1 eV belong to Co^{2+} [28]. The S 2p spectrum is decomposed into three types of peaks, which are metal-sulfur bonds (S $2p_{3/2}$ 161.5 eV, S $2p_{1/2}$ 162.5 eV), surface sulphur ions (163.7 eV), and surface oxidized sulfate species (168.6 eV) [29]. The NITRR properties of CoP/NF and Co_9S_8/NF were also evaluated under the same conditions as the Co_4N/NF electrocatalyst described above. As revealed by the LSV curves in Fig. S20 (Supporting information), both CoP/NF and Co_9S_8/NF exhibit increased current density in the presence of NO_3^-. However, the current density of CoP/NF is significantly higher than that of Co_9S_8/NF at the same cathodic overpotential. The Faraday efficiencies, NH_3 yield rate, conversion rate of NO_3^-, and NH_3 selectivity of CoP/NF and Co_9S_8/NF at different potentials are recorded in Fig. S21 (Supporting information). The Faradaic efficiency presents a volcanic shape curve while the NH_3 yield rate, conversion rate of NO_3^- and NH_3 selectivity gradually increase. It can be clearly observed that the Faradaic efficiency (92.2%), NH_3 yield rate (0.1823 mmol h^{-1} cm^{-2}), conversion rate of NO_3^- (71.2%), and NH_3 selectivity (95.2%) of CoP/NF are apparently higher than those of Co_9S_8/NF (49.4%, 0.0157 mmol h^{-1} cm^{-2}, 9.1%, and 62.5%) at −0.44 V *vs.* RHE. The superior nitrate reduction activity may be due to the changes of CoP/NF revealed by XPS before and after NITRR tests similar to those of Co_4N/NF. As shown in Fig. S22 (Supporting information), the binding energy of Co 2p appears obviously negative shifts while the P/Co atomic ratio decreases from 3.381 to 0.324 after NITRR. Interestingly, with regard to Co_9S_8/NF (Fig. S23 in Supporting information), the Co 2p and S 2p XPS spectra show no obvious change after NITRR tests (S/Co atomic ratio increases from 1.603 to 1.676). XAS further reflected the changes of oxidation state and coordination situation of Co and the dissolution status of P and S species in CoP/NF and Co_9S_8/NF. Fig. S24a (Supporting information) presents the Co K-edge XANES spectra of CoP and post-test CoP, and it is observed that the absorption threshold position of CoP shifts negatively after NITRR tests, suggesting a slightly reduced oxidation state of Co in CoP. The EXAFS spectra of CoP before and after NITRR tests are shown in Fig. S24b (Supporting information), the prominent peak at about 1.8 Å can be ascribed to the Co-P peak [30,31]. After NITRR tests, the intensity of the Co-P peak decreases, indicating that the coordination number of Co decreases because of the leaching of P atoms, which is a strong proof of the formation of P vacancies. However, we can clearly find that the cobalt K-edge XANES spectra of Co_9S_8 before and after NITRR tests almost completely overlap, which manifests the oxidation state of Co_9S_8 remains unchanged during the catalytic process (Fig. S25a in Supporting information). In addition, the main peak located at 1.85 Å is well matched with Co-S [32], and it is worth mentioning that the coordination environment of Co remains stable and unchanged, which matches well with the results of XPS (Fig. S25b in Supporting information). The above discussion strongly proves that the excellent NITRR activities of Co_4N/NF and CoP/NF originate from the nonmetallic vacancies induced by the leaching of N and P atoms, respectively. On the contrary, the poor activity of Co_9S_8/NF is due to the difficulty in breaking the Co-S bond during the electrochemical reduction, resulting in almost no leaching of sulfur species and difficult formation of S vacancies. In conclusion, nonmetallic vacancies induced by *in-situ* nonmetal leaching can effectively improve the performance of NITRR.

To further illustrate the role of nonmetallic vacancies, we artificially introduced sulfur vacancies for Co_9S_8/NF to generate V_S-Co_9S_8/NF by plasma engraving. As illustrated in Fig. S26 (Supporting information), a stronger EPR signal at $g = 2.0034$ in V_S-Co_9S_8 is detected after plasma engraving, indicating that more sulfur vacancies are introduced into V_S-Co_9S_8/NF compared with Co_9S_8/NF [33,34]. As shown in Fig. S27a (Supporting information), the LSV curve of V_S-Co_9S_8/NF shows an obvious increase of current density compared with Co_9S_8/NF in the presence of NO_3^-. With the negative shift of the cathode overpotential, the Faraday efficiency and selectivity gradually increase until the potential reaches −0.44 V *vs.* RHE, and then drop slowly, while the change trend of NH_3 yield rate is the same as that of NO_3^- conversion rate (Figs. S27b and c in Supporting information). The Faraday efficiency and selectivity reach their respective maximum values (83.5%, 83.2%) at −0.44 V *vs.* RHE. V_S-Co_9S_8/NF shows excellent electrochemical NITRR performance, much higher than Co_9S_8/NF (Fig. S27d in Supporting information). The above results confirm that the sulfur vacancies in V_S-Co_9S_8/NF contribute to the improvement of nitrate reduction activity, which further explains the role of nonmetallic vacancies in NITRR.

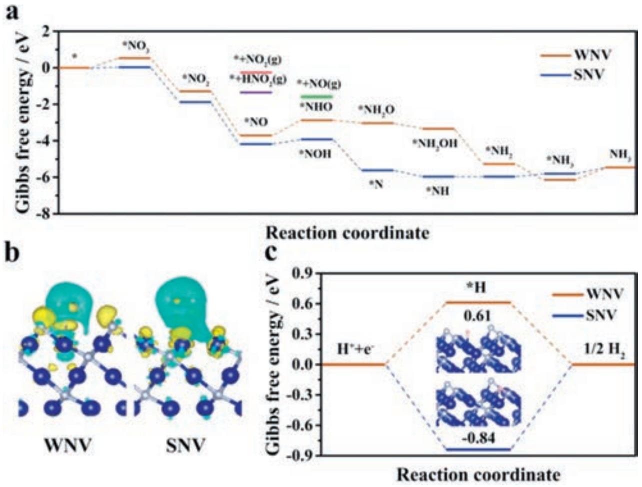

Fig. 4. (a) Calculated Gibbs free energies of different intermediates and byproducts on WNV and SNV Co_4N (111) surfaces toward NITRR. (b) The charge density difference of NH_3 on WNV and SNV Co_4N (111) surfaces. The cyan and yellow isosurfaces represent charge depletion and accumulation, respectively. The isosurface is set to 0.001 e/Å^3. (c) Calculated Gibbs free energies for HER on WNV and SNV Co_4N (111) surfaces.

DFT calculations were conducted to rationalize the nonmetallic vacancies enhanced mechanism caused by nonmetal leaching under *in-situ* electrochemical reduction. The (111) surface of Co_4N was selected for DFT calculations based on investigations of XRD, HRTEM and SEAD. The combined results of these three characterizations indicate that the (111) surface appears as the main exposed surface. Co_4N without NVs (marked as WNV) and with single nitrogen vacancy (SNV) were considered as models since NVs were detected after NITRR tests. Six possible NITRR pathways on Co_4N were considered based on previous reports (Fig. S28 in Supporting information) [35–37]. The optimized models of different intermediates involved in the six reaction pathways are presented in Figs. S29 and S30 (Supporting information). The Gibbs free energies of all the intermediates were calculated to determine the optimal reaction pathway. On WNV, pathway 6 (Fig. S28) is thermodynamically more favorable than the other pathways owing to a lower ΔG from *NO to *NHO (0.83 eV) compared to *NO to *NOH (1.55 eV), simultaneously, *NHO hydrogenation to form $*NH_2O$ is exothermic (Fig. S31a in Supporting information). On SNV, pathway 3 (Fig. S28) is preferred due to the exothermic properties of *NOH reduction to *N (Fig. S31b in Supporting information). The respective optimal pathways are plotted in Fig. 4a for better comparison. Nitrate reduction to ammonia is essentially a series of deoxidation and hydrogenation steps. On SNV, the ΔG of NO_3^- adsorption process is 0.03 eV, which is significantly smaller than that on WNV (0.53 eV), indicating that the presence of nitrogen vacancy contributes to the activation and further reduction of NO_3^-. For NITRR, the hydrogenation step on *NO intermediate plays a crucial role, which can be divided into N-side and O-side. On WNV, the free energy change of the key hydrogenation step (*NO to *NHO) is 0.83 eV, much higher than that of *NO to *NOH (0.32 eV) on SNV, suggesting that *NO can be reduced on SNV more easily. The desorption of NH_3 can be regarded as another important NITRR step. Note that the desorption energy on SNV (0.35 eV) is much lower than that on WNV (0.68 eV), indicating that the desorption process of NH_3 is more likely to occur on the surface of Co_4N with abundant NVs. This is further illustrated by the charge density difference maps of NH_3 adsorbed on the surface of WNV and SNV. As shown in Fig. 4b, an increased electron density between NH_3 and SNV is observed, indicating that the interaction between NH_3 and the surface model is weakened, which is conducive to NH_3 escaping from the catalyst surface [38]. Besides, the potential-determining step (PDS) of WNV is *NO to *NHO (0.83 eV), and the free energy change is also higher than that on SNV ($*NH_3$ to NH_3, 0.35 eV). The high activity of Co_4N catalyst can be explained by the reduced ΔG of the PDS in principle. On SNV, the free energy changes for the release of possible byproducts NO_2, HNO_2 and NO are 1.63, 0.54 and 2.58, respectively, demonstrating that these byproducts are quite difficult to form, thus achieving high NITRR selectivity. In addition, the energy of the HER was also investigated to further interpret the high performance of the Co_4N catalyst (Fig. 4c). The energy required for hydrogen evolution on SNV is 0.84 eV, whereas the adsorption energy of hydrogen atom on the surface of WNV is 0.61 eV. The stronger adsorption of H on the surface of SNV reduces the HER activity, thus inhibiting the production of byproduct H_2. Based on the previously reported literature [39], we infer that *H can facilitate the hydrogenation of *NO to *NOH, thus contributing to the selective conversion of NO_3^- to NH_3, which also explains the difference in potential determination steps between SNV and WNV. The combined results of experiments and theoretical calculations verify that the leaching of nitrogen contributes to the catalytic performance of Co_4N, thus the ultra-high faradaic efficiency of 95.4% and selectivity of 99.4% are obtained.

In conclusion, we developed a high-performance Co_4N/NF electrocatalyst using a facile two-step progress. The Co_4N/NF electrocatalyst displays outstanding activity and selectivity for electrocatalytic reduction of nitrate to ammonia under benign environmental conditions. Such catalyst is demonstrated to exhibit the best catalytic performance at −0.44 V *vs.* RHE with faradaic efficiency and NH_3 selectivity of 95.4% and 99.4%, respectively. A series of comparative experiments manifest that the N atoms are leached from Co_4N and then NVs are introduced, which are responsible for the distinguished performance of ammonia production. Subsequently, DFT calculations were performed to further verify the vacancies enhanced mechanism proposed above. It is found that the NVs on Co_4N can adjust the adsorption intensity of reactant/intermediates to optimize the reaction pathway. Moreover, NVs can modulate the adsorption energy of hydrogen atoms, and *H is more likely to be generated on the surface of SNV, which is beneficial to the production of ammonia. This study highlights a novel *in-situ* nonmetal leaching strategy to design Co-based NITRR electrocatalysts with high NH_3 Faraday efficiency and selectivity, and provides in-depth insights into the vacancy-enhanced NITRR mechanism.

Declaration of competing interest

There are no conflicts to declare.

Acknowledgments

We acknowledge the financial supports from National Natural Science Foundation of China (Nos. 91741105, 22006120), Program for Innovation Team Building at Institutions of Higher Education in Chongqing (No. CXTDX201601011), and Chongqing Municipal Natural Science Foundation (No. cstc2018jcyjAX0625).

Supplementary materials

Supplementary material associated with this article can be found, in the online version, at doi:10.1016/j.cclet.2023.108341.

References

[1] Z. Gao, Y. Zhang, D. Li, et al., J. Hazard. Mater. 286 (2015) 425–431.
[2] J. Martínez, A. Ortiz, I. Ortiz, Appl. Catal. B: Environ. 207 (2017) 42–59.
[3] F. Ni, Y. Ma, J. Chen, W. Luo, J. Yang, Chin. Chem. Lett. 32 (2021) 2073–2078.
[4] Y. Wang, W. Zhou, R. Jia, Y. Yu, B. Zhang, Angew. Chem. Int. Ed. 59 (2020) 5350–5354.
[5] S.L. Foster, S.I.P. Bakovic, R.D. Duda, et al., Nat. Catal. 1 (2018) 490–500.
[6] Y. Ashida, K. Arashiba, K. Nakajima, Y. Nishibayashi, Nature 568 (2019) 536–540.
[7] X. Zhao, G. Hu, F. Tan, et al., J. Mater. Chem. A 9 (2021) 23675–23686.
[8] Y. Yao, J. Wang, U.B. Shahid, et al., Electrochem. Energ. Rev. 3 (2020) 239–270.
[9] Z. Du, J. Liang, S. Li, et al., J. Mater. Chem. A 9 (2021) 13861–13866.
[10] L. Wang, M. Xia, H. Wang, et al., Joule 2 (2018) 1055–1074.
[11] H. Jin, L. Li, X. Liu, et al., Adv. Mater. 31 (2019) 1902709.
[12] X. Zou, J. Xie, C. Wang, et al., Chin. Chem. Lett. 34 (2023) 107908.
[13] T. Feng, F. Li, X. Hu, Y. Wang, Chin. Chem. Lett. 34 (2023) 107862.
[14] R. Jia, Y. Wang, C. Wang, et al., ACS Catal. 10 (2020) 3533–3540.
[15] H. Wang, Y. Guo, C. Li, et al., ACS Appl. Mater. Interfaces 14 (2022) 34761–34769.
[16] Y. Huang, J. Long, Y. Wang, et al., ACS Appl. Mater. Interfaces 13 (2021) 54967–54973.
[17] G. Huang, Z. Xiao, R. Chen, S. Wang, ACS Sustain. Chem. Eng. 6 (2018) 15954–15969.
[18] Z. Wang, G. Qu, C. Wang, et al., Nanoscale 12 (2020) 18400–18408.
[19] L. Wang, W. Zhang, X. Zheng, et al., Nat. Energy 2 (2017) 869–876.
[20] X. Yang, S. Kattel, J. Nash, et al., Angew. Chem. Int. Ed. 58 (2019) 13768–13772.
[21] X. Yang, J. Nash, J. Anibal, et al., J. Am. Chem. Soc. 140 (2018) 13387–13391.
[22] S.Z. Andersen, V. Čolić, S. Yang, et al., Nature 570 (2019) 504–508.
[23] L. Zhang, L.X. Ding, G.F. Chen, X. Yang, H. Wang, Angew. Chem. Int. Ed. 58 (2019) 2612–2616.
[24] C. Wang, W. Zhou, Z. Sun, et al., J. Mater. Chem. A 9 (2021) 239–243.
[25] W. Wang, H. Zhang, S. Zhang, et al., Angew. Chem. Int. Ed. 58 (2019) 16644–16650.
[26] Y. Sun, K. Mao, Q. Shen, et al., Adv. Funct. Mater. 32 (2022) 2109792.
[27] K. Xu, H. Cheng, H. Lv, et al., Adv. Mater. 30 (2018) 1703322.
[28] E.S. Goda, A. ur Rehman, B. Pandit, et al., Chem. Eng. J. 428 (2022) 132470.
[29] Y. Wang, Z. Meng, X. Gong, et al., Chem. Eng. J. 431 (2022) 133980.
[30] Y.N. Zhou, W.H. Hu, Y.N. Zhen, et al., Appl. Catal. B: Environ. 309 (2022) 121230.
[31] Y. Pan, K. Sun, S. Liu, et al., J. Am. Chem. Soc. 140 (2018) 2610–2618.
[32] Y. Li, R. Cao, L. Li, et al., Small 16 (2020) 1906735.
[33] J. Wu, W. Zhong, C. Yang, et al., Appl. Catal. B: Environ. 310 (2022) 121332.
[34] D. Jia, L. Han, Y. Li, et al., J. Mater. Chem. A 8 (2020) 18207–18214.
[35] J. Wang, C. Cai, Y. Wang, et al., ACS Catal. 11 (2021) 15135–15140.
[36] T. Hu, C. Wang, M. Wang, C.M. Li, C. Guo, ACS Catal. 11 (2021) 14417–14427.
[37] Y. Wang, H. Li, W. Zhou, et al., Angew. Chem. Int. Ed. 61 (2022) e202202604.
[38] J. Qin, K. Wu, L. Chen, et al., J. Mater. Chem. A 10 (2022) 3963–3969.
[39] Y. Han, X. Zhang, W. Cai, et al., J. Colloid Interface Sci. 600 (2021) 620–628.